ACS APPLIED MATERIALS & INTERFACES

Research Article

www.acsami.org

Structural and Electrochemical Study of Hierarchical $LiNi_{1/3}Co_{1/3}Mn_{1/3}O_2$ Cathode Material for Lithium-Ion Batteries

Li Li,[†,‡] Lecai Wang,[†] Xiaoxiao Zhang,[†] Man Xie,[†] Feng Wu,[†,‡] and Renjie Chen*[,†,‡]

[†]School of Materials Science & Engineering, Beijing Key Laboratory of Environmental Science and Engineering, Beijing Institute of Technology, Beijing 100081, China

[‡]Collaborative Innovation Center of Electric Vehicles in Beijing, Beijing 100081, China

ABSTRACT: In this study, a facile nanoetching-template route is developed to synthesize porous nanomicrohierarchical $LiNi_{1/3}Co_{1/3}Mn_{1/3}O_2$ microspheres with diameters below 1.5 μm, using porous $CoMnO_3$ binary oxide microspheres as the template. The unique morphology of $CoMnO_3$ template originates from the contraction effect during the oxidative decomposition of $Ca_{0.2}Mn_{0.4}Co_{0.4}CO_3$ precursors and is further improved by selectively removing calcium carbonate with a nanoetching process after calcination. The as-synthesized $LiNi_{1/3}Co_{1/3}Mn_{1/3}O_2$ microsphere, composed of numerous primary particles and pores with size of dozens of nanometers, illustrates a well-assembled porous nanomicrohierarchical structure. When used as the cathode material for lithium-ion batteries, the as-synthesized microspheres exhibit remarkably enhanced electrochemical performances with higher capacity, excellent cycling stability, and better rate capability, compared with the bulk counterpart. Specifically, hierarchical $LiNi_{1/3}Co_{1/3}Mn_{1/3}O_2$ achieves a high discharge capacity of 159.6 mA h g^{-1} at 0.2 C with 98.7% capacity retention after 75 cycles and 133.2 mA h g^{-1} at 1 C with 90% capacity retention after 100 cycles. A high discharge capacity of 135.5 mA h g^{-1} even at a high current of 750 mA g^{-1} (5 C) is also achieved. The nanoetching-template method can provide a general approach to improve cycling stability and rate capability of high capacity cathode materials for lithium-ion batteries.

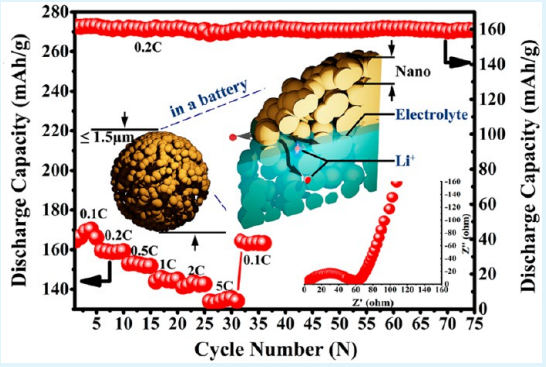

KEYWORDS: *nanomicrohierarchical, nanoetching-template, mesopores, cathode, lithium-ion battery*

1. INTRODUCTION

Over the past decades, the importance of efficient and green energy storage has grown tremendously, primarily impelled by concerns over depletion of fossil fuels, global warming, and increasing demand for durational portable electronics and grid storage systems.[1−3] Among the options, lithium-ion battery (LIB) technology has been the main force to power revolutions in portable electronics market (such as advances of smart cell phones, laptops, and digital cameras) since it was commercialized in 1990s, as lithium-ion battery has the highest gravimetric and volumetric energy densities within all secondary batteries.[4−10] In addition to the constant demands from portable electronics, light, safe, inexpensive, and long-lived hybrid or fully electric vehicles powered by batteries will be required to cut CO_2 emissions from road transport.[1−3,11] Meanwhile, the intrinsic intermittency of renewable energy sources (such as solar and wind power) will require storage facilities in power grids on a large-scale.[1−3,11]

To further develop one of the most potential energy storage technologies, exploration of high-energy-density cathode materials for LIBs plays a key role.[12] In recent years, olivine $LiFePO_4$, spinel $LiMn_2O_4$, and Li-Mn-rich layered oxides have gained a lot of attention from materials chemists. However, energy density of the first two materials is low, due to the low voltage of $LiFePO_4$ (3.4 V) and low capacity for $LiMn_2O_4$ (110 mA g^{-1}).[12,13] The structures of Li-rich materials are still ambiguous, and these materials undergo voltage/capacity decay while cycling, which discourages practical use of these high-energy-density (1000 Wh kg^{-1}) materials.[14,15] In the meantime, the $LiNi_xCo_yMn_{1-x-y}O_2$ family, characterized for high discharge capacity, moderate voltage platform, low cost, and low environmental toxicity, has also been considered as promising cathode candidates.[13−18] Specifically, $LiNi_{1/3}Co_{1/3}Mn_{1/3}O_2$ adopts a rhombohedral α-$NaFeO_2$ structure ($R\bar{3}m$) with consecutively alternating $[MO_2]^-$ (M = Ni, Co, Mn) and Li^+ layers.[19] Initial state of each transition element in the $LiNi_{1/3}Co_{1/3}Mn_{1/3}O_2$ compound is Ni^{2+}, Co^{3+}, and Mn^{4+}, respectively.[20] During charge/discharge, only Ni^{2+} and Co^{3+} of the three are electrically active, involved in Ni^{2+}/Ni^{4+} and Co^{3+}/Co^{4+} redox reactions.[20] Electrochemically inactive Mn^{4+} is beneficial for stability of the crystal structure, reducing Mn dissolution and Jahn−Teller distortion.[12]

Meanwhile, scientists have been controlling and expanding properties of materials by introducing nanoreplacers in many

Received: July 20, 2015
Accepted: September 15, 2015
Published: September 15, 2015

DOI: 10.1021/acsami.5b06584
ACS Appl. Mater. Interfaces 2015, 7, 21939−21947

fields for decades (such as drug delivery, super paramagnetics, and solar hydrogen generation).[21−26] As the size of the materials decreases, both percentage of surface atoms and ratio of surface-to-volume will increase dramatically.[27−29] For instance, a 100 nm particle owns less than 0.2% of atoms on its surface, while a 2 nm particle owns around 90%. It is noteworthy that the surface atoms tend to have one or more dangling bonds to be combined, resulting in increased chemical activity compared to their bulk counterparts.[30] Correspondingly, electrode reactions involve physical interaction and/or chemical reaction at the surface or interface, so the surface energy, specific surface area, and surface chemistry are very important. Moreover, nanomaterials offer much higher mechanical strength than their bulk counterparts, for reduced defects.[30,31] Therefore, nanosized particles are stable under physical strain. Besides size of a particle, porosity, especially mesoporosity, is also an important factor when morphology is associated with functionality of the interface.[32] Due to advantages such as large surface area, enhanced accessibility and the ability to anchor different functional chemicals on their surface, porous materials are ubiquitous.[32] When it comes to $LiNi_{1/3}Co_{1/3}Mn_{1/3}O_2$ preparation, several methods have been reported such as the solid-state method, molten salt method, sol−gel method, and coprecipitation method.[33−39] The resultant products are usually composed of irregular nanoscale or microscale particles or microparticles composed of bulk components.

Herein, we designed a facile nanoetching-template synthesis route to assign a porous nanomicrohierarchical morphology for $LiNi_{1/3}Co_{1/3}Mn_{1/3}O_2$ particles. The spherical appearance of the microparticles was first developed in the coprecipitation process. Porosity of the particles originated from the contraction effect during the oxidative decomposition of the coprecipitate precursors and was further improved by selectively removing calcium carbonate with a nanoetching process. Attributed to the etching process, nanosized primary particles were also successfully developed for the microspheres in this design. When used as cathode material, hierarchical $LiNi_{1/3}Co_{1/3}Mn_{1/3}O_2$ shows significant improvement in electrochemical performances compared with that of the bulk counterpart.

2. EXPERIMENTAL SECTION

2.1. Material Preparation. Porous nanomicrohierarchical $LiNi_{1/3}Co_{1/3}MnO_{1/3}O_2$ microspheres were synthesized by heating Li and Ni into porous $CoMnO_3$ microsphere templates with a solid-state method to form layered crystal structure, barely damaging the morphology of $CoMnO_3$ templates. While, $CoMnO_3$ templates were outcomes of triple carbonate precipitate $Ca_{0.2}Co_{0.4}Mn_{0.4}CO_3$ after decomposition, etching and calcining. Main chemical equations of the synthesis are as follows:

$$Mn(NO_3)_2(aq) + Co(NO_3)_2(aq) + Ca(NO_3)_2(aq) + NH_4HCO_3(aq) \rightarrow Ca_{0.2}Co_{0.4}Mn_{0.4}CO_3\downarrow \quad (1)$$

$$Ca_{0.2}Co_{0.4}Mn_{0.4}CO_3 \xrightarrow{\Delta} CoMnO_3{\cdot}0.5CaCO_3 \quad (2)$$

$$CoMnO_3{\cdot}0.5CaCO_3 + HCl_{(aq)} \rightarrow CoMnO_3 \quad (3)$$

$$CoMnO_3 + Ni(NO_3)_2{\cdot}6H_2O + LiNO_3 \xrightarrow{\Delta} LiNi_{1/3}Co_{1/3}Mn_{1/3}O_2 \quad (4)$$

To fabricate cocarbonate spheres, 15 mmol of $Mn(NO_3)_2{\cdot}4H_2O$, $Co(NO_3)_2{\cdot}6H_2O$, and $Ca(NO_3)_2{\cdot}4H_2O$ (in a molar ratio of 2:2:1) were dissolved in 200 mL of distilled water, which was denoted as solution A. A 100 mmol portion of NH_4HCO_3 was dissolved in 200 mL distilled water to form solution B. A 50 mL portion of ethanol was added slowly to solution A under vigorous stirring. Subsequently, solution B was pumped into solution A, and the suspension was kept at room temperature for 2 h. Meanwhile, lilac carbonate spheres formed. After being gathered by filtration and washed several times with distilled water and ethanol, the carbonate spheres were dried at 60 °C overnight.

Then, $Ca_{0.2}Co_{0.4}Mn_{0.4}CO_3$ spheres were heated at 2 °C min^{-1} to 600 °C for 5 h with the purpose of decomposition of transition metal salt. Afterward, the imbedded $CaCO_3$ was etched with dilute hydrochloric acid, leaving cavities at preoccupied positions. Washed with distilled water and ethanol for several times, porous $CoMnO_3$ microspheres were calcined again for structural stabilization with the same temperature control process above.

To ultimately obtain hierarchical $LiNi_{1/3}Co_{1/3}Mn_{1/3}O_2$, 15 mmol of $Ni(NO_3)_2{\cdot}6H_2O$ and 58 mmol of $LiNO_3$ (with Li excess of 7%) were dispersed in 50 mL of absolute ethanol. A 10 mmol portion of $CoMnO_3$ microspheres was added slowly into the solution, followed by 20 min of stirring. Then, the solvent was evaporated entirely at 60 °C. The remaining dried mixture was ground manually for 10 min and then heated at 2 °C min^{-1} to 900 °C for 10 h. After cooling to room temperature, hierarchical $LiNi_{1/3}Co_{1/3}Mn_{1/3}O_2$ is formed, and the sample is denoted as p-NCM.

For comparison, a deprived process without $Ca(NO_3)_2{\cdot}4H_2O$ participation was performed to synthesize bulk $LiNi_{1/3}Co_{1/3}Mn_{1/3}O_2$ counterpart, which is denoted as b-NCM.

2.2. Material Characterization. A field emission scanning (FESEM, FEI, Quanta 200f), a specific surface area and pore size analyzer (ASIQM000-1-MP), and a transmission electron microscopy (TEM, JEM-2100f) were used to characterize morphologies of the prepared samples. Structural analysis was carried out on an X-ray diffraction facility (XRD; Rigaku Ultima IV-185) with a Cu Kα radiation source. Element mappings of the synthesized samples were carried out with an energy dispersive X-ray detector (EDX). X-ray photoelectronic spectrometer (XPS, VGESCA-LABMK II) was used to determine the ion valence states in the metal oxide.

2.3. Electrochemical Tests. Electrochemical tests were performed under ambient temperature by assembling two-electrode coin cells (type: 2025). In this case, lithium metal served as both the reference electrode and the counter electrode. Meanwhile, the working electrode was composed of 80 wt % active material, 10 wt % conductivity agent (acetylene black), and 10 wt % binder (polyvinylidene difluoride, PVDF), with an aluminum foil current collector. A lithium salt solution, 1 M $LiPF_6$ in a mixture of dimethyl carbonate (DMC), ethylene carbonate (EC), and diethyl carbonate (DEC) equally in volume, was used as the electrolyte. Cell assembly was carried out in a glovebox filled with argon, maintaining both oxygen and moisture content below 1 ppm. Galvanostatic charge/discharge tests were implemented on a battery tester (LAND-CT2001A) with a voltage widow of 2.8−4.3 or 2.5−4.6 V at selected current rates. Cyclic voltammetry (CV) tests were carried out on a CHI660d electrochemical workstation with the voltage window 2.5−4.6 V. Electrochemical impedance spectroscopy (EIS) tests were also carried out on a CHI660d at the frequency range 0.1 MHz to 0.01 Hz with an ac perturbation signal of 5 mV.

3. RESULTS AND DISCUSSION

3.1. Morphology Observation. To obtain the $LiNi_{1/3}Co_{1/3}Mn_{1/3}O_2$ microspheres with a well-defined nano/microhierarchical structure composed of numerous nanosized primary particles and pores, we designed a facile nanoetching-template route, using morphologically modified porous $CoMnO_3$ binary oxide microspheres as the templates. Detailed description was presented in the Experimental Section. To be concise, the synthesis route is illustrated schematically in Scheme 1.

DOI: 10.1021/acsami.5b06584
ACS Appl. Mater. Interfaces 2015, 7, 21939−21947

Scheme 1. Illustration for the Designed Route To Synthesize Hierarchical $LiNi_{1/3}Co_{1/3}Mn_{1/3}O_2$ and the Morphological Effects of the As-Synthesized Material

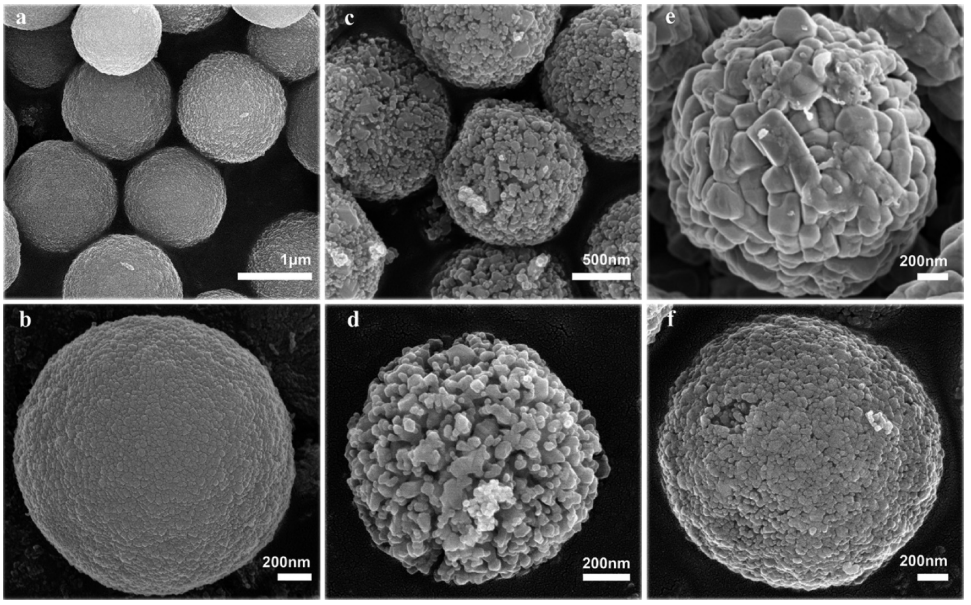

Figure 1. SEM images of $Ca_{0.2}Mn_{0.4}Co_{0.4}CO_3$ microsphere precursors (a, b) and porous $CoMnO_3$ microspheres (c, d) after calcinations at 600 °C for 5 h; SEM images of a single bulk $LiNi_{1/3}Co_{1/3}Mn_{1/3}O_2$ microsphere (e) and a porous nanomicro hierarchical $LiNi_{1/3}Co_{1/3}Mn_{1/3}O_2$ microspheres (f).

Morphology and structural features of carbonate spheres, $CoMnO_3$ templates, and $LiNi_{1/3}Co_{1/3}Mn_{1/3}O_2$ products are confirmed by SEM observations presented in Figure 1. Figure 1a,b shows the images of $Ca_{0.2}Co_{0.4}Mn_{0.4}CO_3$ spheres at different magnifications, indicating formation of uniform microspheres with diameters below 1.5 μm. Notably, uniform $Ca_{0.2}Co_{0.4}Mn_{0.4}CO_3$ microspheres could only form with carefully adjusted conditions such as solution concentration, stirring intensity, and injection speed of NH_4HCO_3 solution. Conditions mentioned above as well as Ca mole fraction could also affect the synthesis in other ways, such as morphology, component, and integrity of $CoMnO_3$ templates. We speculated that the conditions mentioned above could influence element distribution in the carbonate and, subsequently, change the bonding pattern between oxide phase and $CaCO_3$ phase when the carbonate precipitate was calcined. However, a firm $CoMnO_3$ template should be composed of continuous oxide phase as a whole without a portion separated by a $CaCO_3$ phase. On the other hand, $CaCO_3$ should not be wrapped by oxide phases entirely, or it would lead to $CaCO_3$ residual. SEM images of $CoMnO_3$ templates at different magnifications were presented in Figure 1c,d. $CoMnO_3$ templates exhibit a spheroidal shape in microscale and contain numerous nano-sized branches and pores, nearly without shedding fragments. The unique morphology and structural features are attributed to a synergic effect of the contraction generated during the oxidative decomposition of $Ca_{0.2}Mn_{0.4}Co_{0.4}CO_3$ precursors and the $CaCO_3$ deprivation process. Similar features were also

DOI: 10.1021/acsami.5b06584
ACS Appl. Mater. Interfaces 2015, 7, 21939−21947

found in $LiNi_{1/3}Co_{1/3}Mn_{1/3}O_2$ products presented in Figure 1f, but more building blocks and smaller pores emerge. Compared to the bulk counterpart (Figure 1e), porous $LiNi_{1/3}Co_{1/3}Mn_{1/3}O_2$ is composed of much smaller primary particles (about 25 nm in width).

Nitrogen adsorption/desorption tests were further carried out to evidence the porosity of hierarchical $LiNi_{1/3}Co_{1/3}Mn_{1/3}O_2$ (Figure 2). The average BJH pore diameter of 37.56 nm and two peaks sitting at 2.44 and 31.7 nm indicate that the pores are mainly mesopores. Large-surface BET area with a value of 51.77 $m^2\ g^{-1}$ is also observed. As a conclusion, a porous microstructure assembled with nanosized building blocks is established for the $LiNi_{1/3}Co_{1/3}Mn_{1/3}O_2$ compound, which matches well with our original design.

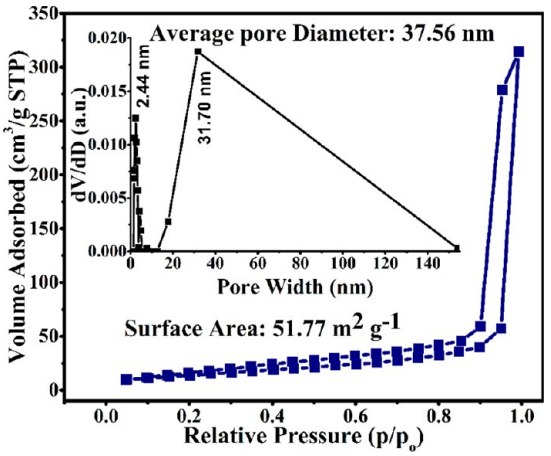

Figure 2. Nitrogen adsorption/desorption isotherms and BJH pore size distribution of hierarchical $LiNi_{1/3}Co_{1/3}Mn_{1/3}O_2$.

3.2. Structure and Composition Analysis. To gain more insight into as-synthesized hierarchical $LiNi_{1/3}Co_{1/3}Mn_{1/3}O_2$ and $CoMnO_3$ templates, XRD, TEM, EDX, and XPS measurements were also performed. XRD patterns of the as-synthesized $LiNi_{1/3}Co_{1/3}Mn_{1/3}O_2$ are presented in Figure 3. Sharp and well-defined peaks in the patterns indicate that the obtained compound was well-crystallized. All peaks can be indexed to a hexagonal α-$NaFeO_2$ structure (space group: $R\bar{3}m$) without any impurities. The distinct (006)/(102) and (108)/(110) splitting peaks suggest the formation of a highly ordered hexagonal layered structure. Intensity ratio of the (003) and (104) peaks ($I_{(003)}/I_{(104)}$) is 1.41, larger than 1.2, indicating low cation mixing. Lattice parameters of hierarchical $LiNi_{1/3}Co_{1/3}Mn_{1/3}O_2$ were a = 2.862 Å, c = 14.242 Å, and a/c = 0.201. The parameters agree well with reported studies.[20] High c/a value also indicates small cation mixing and good ordering of the transition metal ions in the metal layer. The porous property is once again confirmed by the light and dark low-resolution TEM images (Figure 4a,b). High-resolution TEM (HRTEM) images (Figure 4c,d), showing well-crystalline parallel planes, indicate that both $CoMnO_3$ microspheres and $LiNi_{1/3}Co_{1/3}Mn_{1/3}O_2$ microspheres are structurally uniform and well-crystallized. 2D lattice planes of $CoMnO_3$ microspheres are about 4 Å, matching the (211) planes of Mn_2O_3. From the representative high-resolution TEM image in Figure 4d, lattice spacing of (101) and (003) can be indexed as 2.44 and 4.75 Å for layered $LiNi_{1/3}Co_{1/3}Mn_{1/3}O_2$ with the inclined angle of 80.2°. Composition and internal homogeneity of $CoMnO_3$ and internal homogeneity of as-prepared $LiNi_{1/3}Co_{1/3}Mn_{1/3}O_2$ were further investigated by energy dispersive X-ray spectroscopy (EDX) analysis (Figure 4e–g). According to the results, the transition metals are nearly equal in molar ratio and are uniformly distributed in the particles.

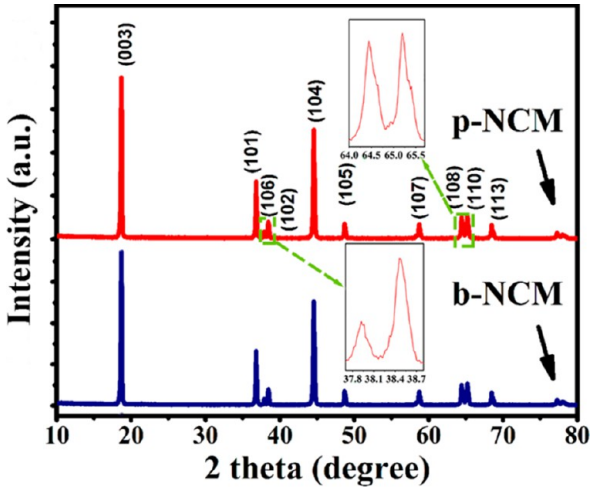

Figure 3. XRD patterns of as-synthesized hierarchical $LiNi_{1/3}Co_{1/3}Mn_{1/3}O_2$ and bulk $LiNi_{1/3}Co_{1/3}Mn_{1/3}O_2$.

To learn more about the valence state of the transition metals in the hierarchical $LiNi_{1/3}Co_{1/3}Mn_{1/3}O_2$ material, XPS measurements were performed. The corresponding results, which have been calibrated by referring the C 1s binging energy to 284.6 eV, are presented in Figure 5. The 854.3, 780.0, and 642.8 eV dominant peaks are attributed to Ni^{2+}, Co^{3+}, and Mn^{4+}, respectively.[35] The Ni 2p XPS spectrum in Figure 5a presents an intense Ni $2p_{3/2}$ peak at about 854.3 eV which is accompanied by a shakeup peak at about 861.0 eV. The specific pattern is characteristic for Ni^{2+}.[36] By using a Gaussian fitting method, a less prominent peak at about 855.8 eV is also observed, indicating the existence of Ni^{3+}.[12] Two major peaks at about 780.0 and 795.0 eV emerge in the Co 2p spectrum (Figure 5b), which are assigned to the Co $2p_{3/2}$ and $2p_{1/2}$ peaks, respectively.[35,36] The existence of Co^{3+} is further confirmed by the two weak satellite peaks at 789.5 and 804.5 eV which are the footprint of Co^{3+}.[37] Meanwhile, two weak peaks at about 781.1 and 796.6 eV indicated the coexistence of Co^{2+}. In the Mn 2p spectrum (Figure 5c), two main spin–orbit lines at about 642.8 eV of $2p_{3/2}$ and 654.4 eV of $2p_{1/2}$ with 11.6 eV separation indicate the majority of Mn^{4+}. However, Mn^{3+} is also indicated by the existence of a pair of less prominent peaks at about 641.8 and 653.3 eV.[38] As reported, the minor contribution of Ni^{3+} and Mn^{3+} is due to the electron transfer between Ni^{2+} and Mn^{4+} ($Ni^{2+} + Mn^{4+} \leftrightarrow Ni^{3+} + Mn^{3+}$).[20] In the present synthesis, the dominant oxidation state of Ni and Mn in the $LiNi_{1/3}Co_{1/3}Mn_{1/3}O_2$ compound is +2 and +4, respectively, while the small fraction of Ni^{3+} and Mn^{3+} is inevitably due to the valence degeneracy. During charge/discharge cycling, the Ni^{2+} and Co^{3+} cations are electrochemically active and undergo redox reactions. The electrochemically inactive Mn^{4+} cation is believed to benefit the stability of the material framework.[39] The O 1s spectra (Figure 5d) for hierarchical $LiNi_{1/3}Co_{1/3}Mn_{1/3}O_2$ contain two oxygen contributions. The peak at 529.2 eV is typical for metal oxygen bonds.[40] The peak sitting at 531.5 eV is associated with oxygen ions in low coordination at the surface.[40]

DOI: 10.1021/acsami.5b06584
ACS Appl. Mater. Interfaces 2015, 7, 21939–21947

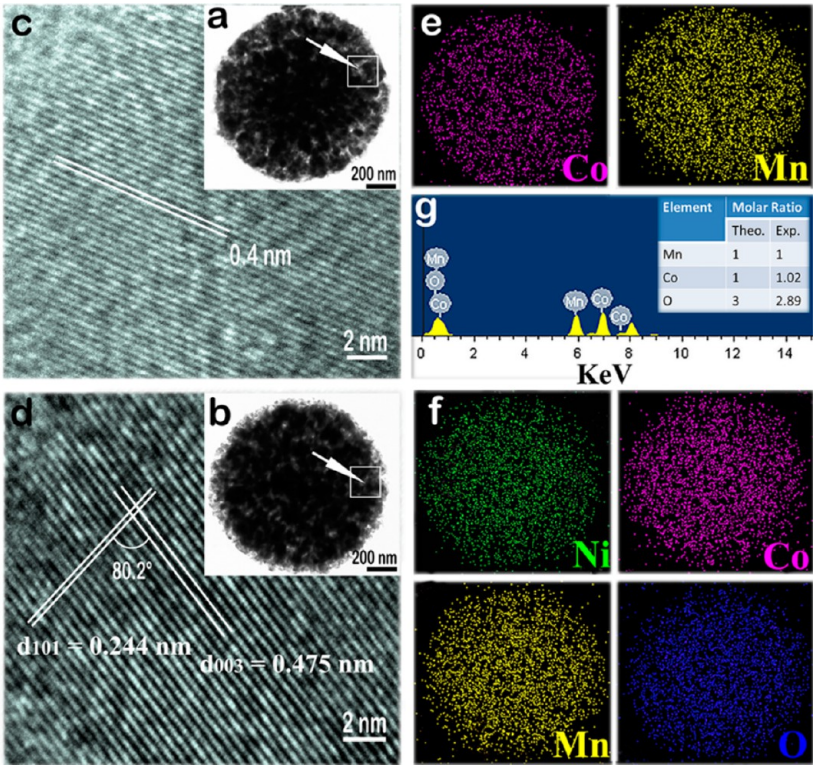

Figure 4. TEM images of a single porous $CoMnO_3$ microsphere (a) and porous nanomicrohierarchical $LiNi_{1/3}Co_{1/3}Mn_{1/3}O_2$ microspheres (b); HRTEM images at the edge of the $CoMnO_3$ microsphere (c) and at the edge of the $LiNi_{1/3}Co_{1/3}Mn_{1/3}O_2$ microsphere (d); element mappings of a $CoMnO_3$ microsphere (e) and a porous nanomicro hierarchical $LiNi_{1/3}Co_{1/3}Mn_{1/3}O_2$ microspheres (f). EDX spectra of $CoMnO_3$ (g); the inset table shows the molar ratios of the Mn, Co, and O elements.

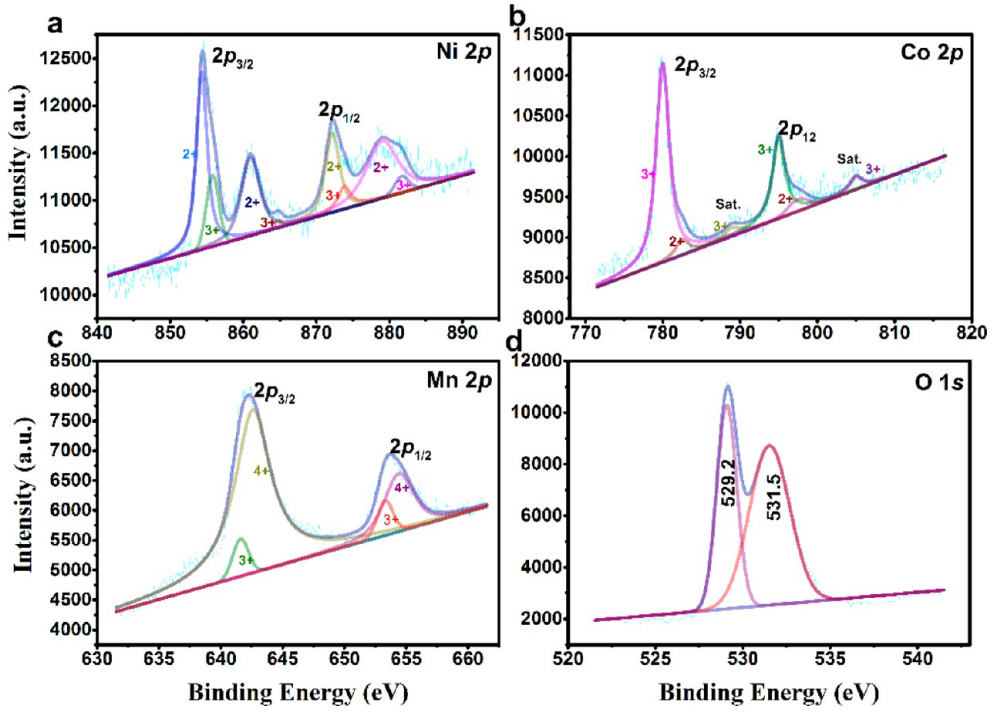

Figure 5. XPS spectra of (a) Ni 2p, (b) Co 2p, (c) Mn 2p, and (d) O 1s for hierarchical $LiNi_{1/3}Co_{1/3}Mn_{1/3}O_2$.

3.3. Electrochemical Performance in Lithium-Ion Battery. The hierarchical structure can increase the utilization of the cathode material and initiate new lithium storage space in mesopores, leading to higher capacity than its bulk counterpart.[41] Second, mesopores and nanosized primary particles assembled in this structure can shorten the Li^+ ion diffusion path and provide larger electrode−electrolyte interface for Li^+ to flux across, which will enhance both the working voltage and the rate capability.[41] Also, the instinctive high mechanical strength of nanoparticles and buffering effect of the porous

DOI: 10.1021/acsami.5b06584
ACS Appl. Mater. Interfaces 2015, 7, 21939−21947

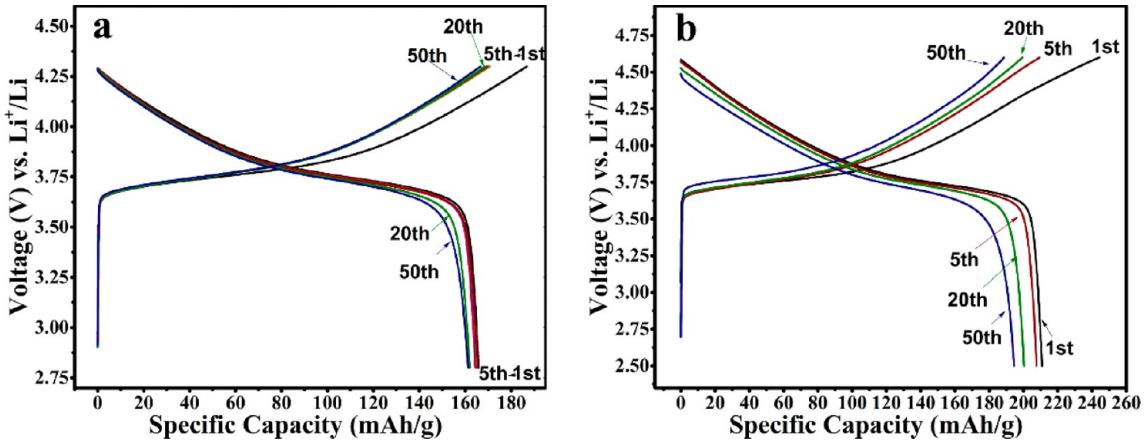

Figure 6. Charge/discharge curves of hierarchical $LiNi_{1/3}Co_{1/3}Mn_{1/3}O_2$ at 0.1 C in the voltage range between 2.8 and 4.3 V (a) and between 2.5 and 4.6 V (b).

structure can promote the cycling stability under the mechanical strain induced by volume change during the repeated Li^+ insertion/extraction processes.[42]

To illustrate electrochemical performance in a low current rate, galvanostatic charge/discharge curves of hierarchical $LiNi_{1/3}Co_{1/3}Mn_{1/3}O_2$ at 0.1 C rate (1C = 150 mA g^{-1}) between 2.8 and 4.3 V are shown in Figure 6a. The midpoint of the plateaus of the charge and discharge curves is around 3.8 V. Before the rapid drop at about 3.5 V in the discharge curves, voltage decrease is quite smooth, which guarantees high energy density. Meanwhile, long platforms of charge and discharge curves are beneficial for electrode stability in practice. Discharge capacity values for the porous microspheres after the 1st, 5th, 20th, and 50th cycles are 165.8, 165.4, 162, and 161.3 mA h g^{-1}, respectively. The 2−5 cycles almost keep the same trace. A small capacity loss of 2.3% is observed after 20 cycles and 3% after 50 cycles. As for a wider voltage range between 2.5 and 4.6 V, discharge capacity values for the porous microspheres after 1st, 5th, 20th, and 50th are 210.8, 207.6, 200.3, and 194.5 mA h g^{-1}, respectively. Notably, observable capacity/voltage fading emerges with the wider voltage range. The dissolution of transition metal ions might take place at high voltage, along with the crystal destruction and the decomposition of electrolyte, leading to severe performance decay.[43]

The contrasting cycling performances of bulk $LiNi_{1/3}Co_{1/3}Mn_{1/3}O_2$ (b-NCM) and hierarchical $LiNi_{1/3}Co_{1/3}Mn_{1/3}O_2$ (p-NCM) at 0.2 and 1 C are shown in Figure 7a,b. Discharge capacities are 159.6 mA h g^{-1} at 0.2 C after 75 cycles and 133.2 mA h g^{-1} at 1 C after 100 cycles for p-NCM. At the same time, b-NCM only achieves 139.8 mA h g^{-1} at 0.2 C after 75 cycles and 112.8 mA h g^{-1} at 1 C after 100 cycles. Obviously, p-NCM delivers more electric energy at the same conditions, although both of them possess a high Coulombic efficiency between 97% and 99%. On the other hand, the smaller slope of p-NCM discharge capacity curves indicates better cycling stability, compared to b-NCM.

Besides high specific capacity and good cycling stability, rate capability is also a very important property for cathode materials. To give the rate capability of prepared materials an inspection, cells were charged at 0.2 C and discharged at various current rates (0.1−5 C). The results are shown in Figure 7c. The discharge capacities for p-NCM electrode are 169.2, 159.6, 153, 145.9, 143.5, and 135.5 mA h g^{-1} at current rates of 0.1, 0.2, 0.5, 1, 2, and 5 C, respectively. Discharge capacity dropped as current rates increase. However, the electrode can still deliver a capacity higher than 133.3 mA h g^{-1} even at 5 C. Besides, the discharge capacity recovers to 164.3 mA h g^{-1}, nearly the same as the value at 0.1 C at the beginning of the test. In contrast, capacity drop of b-NCM is much more drastic when current rate increases. Therefore, the unique porous structure of the microspheres is considered to be responsible for the superior rate capability of p-NCM.

To obtain a more detailed understanding of electrochemical behavior of prepared materials during cycling, cyclic voltammetry curves of p-NCM and b-NCM electrodes between 2.5 and 4.6 V at a scanning rate of 0.1 mV s^{-1} are presented in Figure 7d,f. A pair of redox peaks in the potential range 3.6−3.9 V is found in both electrodes, which correspond well with the features of cyclic voltammetry test reported in the literature.[33] The absence of a reduction peaks at 3.2 V in both curves indicates that there is no reduction of Mn^{3+}/Mn^{4+}. Nickel and cobalt with oxidation states of 2+ and 3+, respectively, are known to be electrochemically active and undergo redox reactions during charge/discharge cycles, whereas manganese with oxidation state of 4+ is inactive. It is believed to be beneficial for the stability of the metal oxide lattice. Except for the first cycle, the followed two curves in the subsequent cycles overlap well, indicating the good reversibility of lithium ions intercalation/deintercalation in the p-NCM. Although both of the electrodes have similar CV curves, the current density of p-NCM is obviously stronger than that of b-NCM, which indicates better electrochemical performance.

The microspheres with connective pores permit electrolyte to flood and transport, which will exert positive effect on kinetic performance of as-assembled cells. Presumably, p-NCM would exert smaller resistance. EIS tests of both p-NCM and b-NCM were performed to verify the prediction. The results were shown in Figure 7e. The impedance spectra of both hierarchical $LiNi_{1/3}Co_{1/3}Mn_{1/3}O_2$ and bulk particle electrodes contain a partial semicircle among high- to medium-frequency region and an inclined line in the low-frequency region. The semicircle in the high- to medium-frequency region can be usually assigned to the charge transfer impedance (R_{ct}), relating to charge transfer through the electrode/electrolyte interface. Also, the quasistraight line in the low-frequency region represents the Warburg impedance, reflecting the solid-state diffusion of Li in the electrode materials.[38,39] According to Figure 7e, porous microspheres (R_{ct} = 54.45 Ω) possess obviously lower charge

DOI: 10.1021/acsami.5b06584
ACS Appl. Mater. Interfaces 2015, 7, 21939−21947

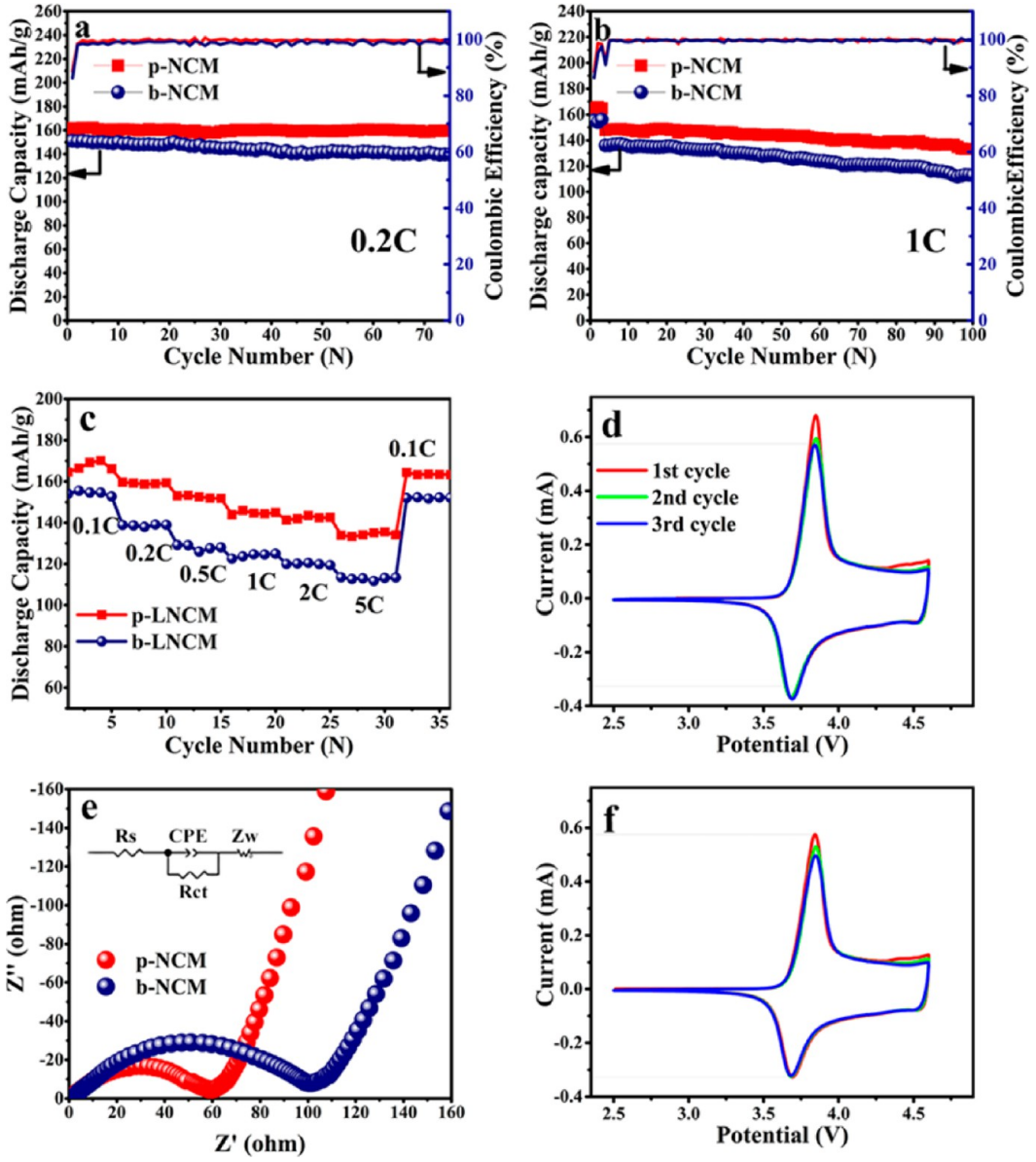

Figure 7. Cycle performances for hierarchical (p-NCM) and bulk (b-NCM) $LiNi_{1/3}Co_{1/3}Mn_{1/3}O_2$ microsphere electrodes at 0.2 C (a) and 1 C (b). Rate performance of hierarchical (p-NCM) and bulk (b-NCM) $LiNi_{1/3}Co_{1/3}Mn_{1/3}O_2$ electrodes (c). Cyclic voltammetry (CV) curves of hierarchical (d) and bulk (f) $LiNi_{1/3}Co_{1/3}Mn_{1/3}O_2$ electrodes in the voltage range 2.5−4.6 V at the scan rate of 0.1 mV s^{-1}. Nyquist plots of hierarchical (p-NCM) and bulk (b-NCM) $LiNi_{1/3}Co_{1/3}Mn_{1/3}O_2$ electrodes in the frequency range from 100 kHz to 0.1 Hz (e).

transfer resistance compared to that of the bulk particles (R_{ct} = 97.36 Ω), in consequence, providing better Li-intercalation kinetic properties.

4. CONCLUSION

In summary, we successfully designed a facile nanoetching-template route to synthesize hierarchical $LiNi_{1/3}Co_{1/3}Mn_{1/3}O_2$ microspheres composed of numerous nanosized pores and primary blocks. The as-synthesized hierarchical $LiNi_{1/3}Co_{1/3}Mn_{1/3}O_2$ shows high capacity, excellent cycling performance, and good rate capability as cathode material for lithium-ion batteries in comparison with the bulk counterpart. On the basis of this work, hierarchical $LiNi_{1/3}Co_{1/3}Mn_{1/3}O_2$ microspheres could be considered as a potential cathode candidate for the future development of lithium-ion batteries. More importantly, the nanoetching-template method developed in this work could also provide an approach to improve cycle stability and rate capability of cathode materials for lithium-ion batteries effectively.

AUTHOR INFORMATION

Corresponding Author

*E-mail: chenrj@bit.edu.cn. Phone: +86 10 68912508. Fax: +86 10 68451429.

Notes

The authors declare no competing financial interest.

ACKNOWLEDGMENTS

The experimental work of this study was supported by the Chinese National 973 Program (2015CB251100), the National Science Foundation of China (NSFC 51302014), Beijing Nova Program (Z121103002512029), and the New Century Educa-

DOI: 10.1021/acsami.5b06584
ACS Appl. Mater. Interfaces 2015, 7, 21939−21947

tional Talents Plan of the Chinese Education Ministry (NCET-12-0050).

REFERENCES

(1) Whittingham, M. S. Materials Challenges Facing Electrical Energy Storage. *MRS Bull.* **2008**, *33*, 411−419.

(2) Dunn, B.; Kamath, H.; Tarascon, J. M. Electrical Energy Storage for the Grid: A Battery of Choices. *Science* **2011**, *334*, 928−935.

(3) Liu, J.; Zhang, J. G.; Yang, Z. G.; Lemmon, J. P.; Imhoff, C.; Graff, G. L.; Li, L. Y.; Hu, J. Z.; Wang, C. M.; Xiao, J.; Xia, G.; Viswanathan, V. V.; Baskaran, S.; Sprenkle, V.; Li, X. L.; Shao, Y. Y.; Schwenzer, B. Materials Science and Materials Chemistry for Large Scale Electrochemical Energy Storage: From Transportation to Electrical Grid. *Adv. Funct. Mater.* **2013**, *23*, 929−946.

(4) Masquelier, C.; Croguennec, L. Polyanionic (Phosphates, Silicates, Sulfates) Frameworks as Electrode Materials for Rechargeable Li (or Na) Batteries. *Chem. Rev.* **2013**, *113*, 6552−6591.

(5) Armand, M.; Tarascon, J. M. Building Better Batteries. *Nature* **2008**, *451*, 652−657.

(6) Bruce, P. G.; Freunberger, S. A.; Hardwick, L. J.; Tarascon, J. M. Li-O_2 and Li-S Batteries with High Energy Storage. *Nat. Mater.* **2012**, *11*, 19−29.

(7) Park, M.; Zhang, X. C.; Chung, M. D.; Less, G. B.; Sastry, A. M. A Review of Conduction Phenomena in Li-Ion Batteries. *J. Power Sources* **2010**, *195*, 7904−7929.

(8) Scrosati, B.; Garche, J. Lithium Batteries: Status, Prospects and Future. *J. Power Sources* **2010**, *195*, 2419−2430.

(9) Goodenough, J. B.; Park, K. S. The Li-Ion Rechargeable Battery: A Perspective. *J. Am. Chem. Soc.* **2013**, *135*, 1167−1176.

(10) Wang, H. L.; Yang, Y.; Liang, Y. Y.; Zheng, G. Y.; Li, Y. G.; Cui, Y.; Dai, H. J. Rechargeable Li-O_2 Batteries with a Covalently Coupled $MnCo_2O_4$-Graphene Hybrid as an Oxygen Cathode Catalyst. *Energy Environ. Sci.* **2012**, *5*, 7931−7935.

(11) Palacin, M. R. Recent Advances in Rechargeable Battery Materials: a Chemist's Perspective. *Chem. Soc. Rev.* **2009**, *38*, 2565−2575.

(12) Li, J. F.; Xiong, S. L.; Liu, Y. R.; Ju, Z. C.; Qian, Y. T. Uniform $LiNi_{1/3}Co_{1/3}Mn_{1/3}O_2$ Hollow Microspheres: Designed Synthesis, Topotactical Structural Transformation and Their Enhanced Electrochemical Performance. *Nano Energy* **2013**, *2*, 1249−1260.

(13) Xu, J. T.; Dou, S. X.; Liu, H. K.; Dai, L. M. Cathode Materials for Next Generation Lithium Ion Batteries. *Nano Energy* **2013**, *2*, 439−442.

(14) Yu, H. J.; Ishikawa, R.; So, Y. G.; Shibata, N.; Kudo, T.; Zhou, H. S.; Ikuhara, Y. Direct Atomic-Resolution Observation of Two Phases in the $Li_{1.2}Mn_{0.567}Ni_{0.166}Co_{0.067}O_2$ Cathode Material for Lithium-Ion Batteries. *Angew. Chem., Int. Ed.* **2013**, *52*, 5969−5973.

(15) Yu, H. J.; Kim, H. J.; Wang, Y. R.; He, P.; Asakura, D.; Nakamura, Y.; Zhou, H. S. High-Energy 'Composite' Layered Manganese-Rich Cathode Materials via Controlling Li_2MnO_3 Phase Activation for Lithium-Ion Batteries. *Phys. Chem. Chem. Phys.* **2012**, *14*, 6584−6595.

(16) Santhanam, R.; Rambabu, B. High Rate Cycling Performance of $Li_{1.05}Ni_{1/3}Co_{1/3}Mn_{1/3}O_2$ Materials Prepared by Sol-Gel and Co-precipitation Methods for Lithium-Ion Batteries. *J. Power Sources* **2010**, *195*, 4313−4317.

(17) Hashem, A. M. A.; Abdel-Ghany, A. E.; Eid, A. E.; Trottier, J.; Zaghib, K.; Mauger, A.; Julien, C. M. Study of the Surface Modification of $LiNi_{1/3}Co_{1/3}Mn_{1/3}O_2$ Cathode Material for Lithium Ion Battery. *J. Power Sources* **2011**, *196*, 8632−8637.

(18) Hwang, B. J.; Tsai, Y. W.; Carlier, D.; Ceder, G. A Combined Computational/Experimental Study on $LiNi_{1/3}Co_{1/3}Mn_{1/3}O_2$. *Chem. Mater.* **2003**, *15*, 3676−3682.

(19) Yabuuchi, N.; Makimura, Y.; Ohzuku, T. Solid-State Chemistry and Electrochemistry of $LiCo_{1/3}Ni_{1/3}Mn_{1/3}O_2$ for Advanced Lithium-Ion Batteries III. Rechargeable Capacity and Cycleability. *J. Electrochem. Soc.* **2007**, *154*, A314−A321.

(20) Huang, Z. D.; Liu, X. M.; Oh, S. W.; Zhang, B. A.; Ma, P. C.; Kim, J. K. Microscopically Porous, Interconnected Single Crystal $LiNi_{1/3}Co_{1/3}Mn_{1/3}O_2$ Cathode Material for Lithium Ion Batteries. *J. Mater. Chem.* **2011**, *21*, 10777−10784.

(21) Murray, C. B.; Kagan, C. R.; Bawendi, M. G. Synthesis and Characterization of Monodisperse Nanocrystals and Close-Packed Nanocrystal Assemblies. *Annu. Rev. Mater. Sci.* **2000**, *30*, 545−610.

(22) Namgung, R.; Lee, Y. M.; Kim, J.; Jang, Y.; Lee, B. H.; Kim, I. S.; Sokkar, P.; Rhee, Y. M.; Hoffman, A. S.; Kim, W. J. Poly-Cyclodextrin and Poly-Paclitaxel Nano-Assembly for Anticancer Therapy. *Nat. Commun.* **2014**, *5*, 3702.

(23) Alivisatos, A. P. Semiconductor Clusters, Nanocrystals, and Quantum Dots. *Science* **1996**, *271*, 933−937.

(24) Roduner, E. Size Matters: Why Nanomaterials are Different. *Chem. Soc. Rev.* **2006**, *35*, 583−592.

(25) Link, S.; El-Sayed, M. A. Shape and Size Dependence of Radiative, Non-Radiative and Photothermal Properties of Gold Nanocrystals. *Int. Rev. Phys. Chem.* **2000**, *19*, 409−453.

(26) Burda, C.; Chen, X. B.; Narayanan, R.; El-Sayed, M. A. Chemistry and Properties of Nanocrystals of Different Shapes. *Chem. Rev.* **2005**, *105*, 1025−1102.

(27) Alivisatos, A. P. Perspectives on the Physical Chemistry of Semiconductor Nanocrystals. *J. Phys. Chem.* **1996**, *100*, 13226−13239.

(28) Chen, X. B.; Li, C.; Gratzel, M.; Kostecki, R.; Mao, S. S. Nanomaterials for Renewable Energy Production and Storage. *Chem. Soc. Rev.* **2012**, *41*, 7909−7937.

(29) Terrones, M. Science and Technology of the Twenty-First Century: Synthesis, Properties and Applications of Carbon Nanotubes. *Annu. Rev. Mater. Res.* **2003**, *33*, 419−501.

(30) Arico, A. S.; Bruce, P.; Scrosati, B.; Tarascon, J. M.; Van Schalkwijk, W. Nanostructured Materials for Advanced Energy Conversion and Storage Devices. *Nat. Mater.* **2005**, *4*, 366−377.

(31) Serrano, E.; Rus, G.; Garcia-Martinez, J. Nanotechnology for Sustainable Energy. *Renewable Sustainable Energy Rev.* **2009**, *13*, 2373−2384.

(32) Linares, N.; Silvestre-Albero, A. M.; Serrano, E.; Silvestre-Albero, J.; Garcia-Martinez, J. Mesoporous Materials for Clean Energy Technologies. *Chem. Soc. Rev.* **2014**, *43*, 7681−7717.

(33) Ohzuku, T.; Makimura, Y. Layered Lithium Insertion Material of $LiNi_{1/2}Mn_{1/2}O_2$: A Possible Alternative to $LiCoO_2$ for Advanced Lithium-Ion Batteries. *Chem. Lett.* **2001**, *30*, 744−745.

(34) Yao, Y. L.; Liu, H. C.; Li, G. C.; Peng, H. R.; Chen, K. Z. Synthesis and Electrochemical Performance of Phosphate-Coated Porous $LiNi_{1/3}Co_{1/3}Mn_{1/3}O_2$ Cathode Material for Lithium Ion Batteries. *Electrochim. Acta* **2013**, *113*, 340−345.

(35) Luo, X. F.; Wang, X. Y.; Liao, L.; Gamboa, S.; Sebastian, P. J. Synthesis and Characterization of High Tap-Density Layered $LiNi_{1/3}Co_{1/3}Mn_{1/3}O_2$ Cathode Material via Hydroxide Co-precipitation. *J. Power Sources* **2006**, *158*, 654−658.

(36) Deng, C.; Liu, L.; Zhou, W.; Sun, K.; Sun, D. Characterization of $Li[Ni_{1/3}Co_{1/3}Mn_{1/3}]O_2$ Synthesized via Salvolatile Coprecipitation for Lithium-Ion Batteries. *Electrochem. Solid-State Lett.* **2007**, *10*, A279−A282.

(37) Lee, J. W.; Lee, J. H.; Viet, T. T.; Lee, J. Y.; Kim, J. S.; Lee, C. H. Synthesis of $LiNi_{1/3}Co_{1/3}Mn_{1/3}O_2$ Cathode Materials by Using a Supercritical Water Method in a Batch Reactor. *Electrochim. Acta* **2010**, *55*, 3015−3021.

(38) Lee, S.; Park, S. S. Atomistic Simulation Study of Mixed-Metal Oxide ($LiNi_{1/3}Co_{1/3}Mn_{1/3}O_2$) Cathode Material for Lithium Ion Battery. *J. Phys. Chem. C* **2012**, *116*, 6484−6489.

(39) Zhao, R. R.; Yang, Z. L.; Chen, J. C.; Chen, Z. J.; Liang, J. X.; Chen, H. Y. Novel Solvo/Hydrothermal Assisted Co-precipitation Method for Faceted $LiNi_{1/3}Mn_{1/3}Co_{1/3}O_2$ Cathode Material. *J. Alloys Compd.* **2015**, *627*, 206−210.

(40) Marco, J. F.; Gancedo, J. R.; Gracia, M.; Gautier, J. L.; Rios, E.; Berry, F. J. Characterization of the Nickel Cobaltite, $NiCo_2O_4$ Prepared by Several Methods: An XRD, XANES, EXAFS, and XPS Study. *J. Solid State Chem.* **2000**, *153*, 74−81.

(41) Zhang, K.; Han, X. P.; Hu, Z.; Zhang, X. L.; Tao, Z. L.; Chen, J. Nanostructured Mn-Based Oxides for Electrochemical Energy Storage and Conversion. *Chem. Soc. Rev.* **2015**, *44*, 699−728.

DOI: 10.1021/acsami.5b06584
ACS Appl. Mater. Interfaces 2015, 7, 21939−21947

(42) Zhang, Q. F.; Uchaker, E.; Candelaria, S. L.; Cao, G. Z. Nanomaterials for Energy Conversion and Storage. *Chem. Soc. Rev.* **2013**, *42*, 3127−3171.
(43) Wang, X. S.; Xing, L. D.; Liao, X. L.; Chen, X. F.; Huang, W. N.; Yu, Q. P.; Xu, M. Q.; Huang, Q. M.; Li, W. S. Improving Cyclic Stability of Lithium Cobalt Oxide Based Lithium Ion Battery at High Voltage by Using Trimethylboroxine as an Electrolyte Additive. *Electrochim. Acta* **2015**, *173*, 804−811.

DOI: 10.1021/acsami.5b06584
ACS Appl. Mater. Interfaces 2015, 7, 21939−21947